Deep Data Analysis of Conductive Phenomena on Complex Oxide Interfaces: Physics from Data Mining

Evgheni Strelcov,[†,⊥] Alexei Belianinov,[†,⊥] Ying-Hui Hsieh,[‡] Stephen Jesse,[†] Arthur P. Baddorf,[†] Ying-Hao Chu,[‡,§] and Sergei V. Kalinin[†,*]

[†]Center for Nanophase Materials Sciences, Oak Ridge National Laboratory, Oak Ridge, Tennessee 37831, United States, [‡]Department of Materials Science and Engineering, National Chiao Tung University, Hsinchu 30010, Taiwan, and [§]Institute of Physics, Academia Sinica, Taipei 105, Taiwan. [⊥]E. Strelcov and A. Belianinov contributed equally to this work.

ABSTRACT Spatial variability of electronic transport in $BiFeO_3$—$CoFe_2O_4$ (BFO—CFO) self-assembled heterostructures is explored using spatially resolved first-order reversal curve (FORC) current voltage (IV) mapping. Multivariate statistical analysis of FORC-IV data classifies statistically significant behaviors and maps characteristic responses spatially. In particular, regions of grain, matrix, and grain boundary responses are clearly identified. *k*-Means and Bayesian demixing analysis suggest the characteristic response be separated into four components, with hysteretic-type behavior localized at the BFO—CFO tubular interfaces. The conditions under which Bayesian components allow direct physical interpretation are explored, and transport mechanisms at the grain boundaries and individual phases are analyzed. This approach conjoins multivariate statistical analysis with physics-based interpretation, actualizing a robust, universal, data-driven approach to problem solving, which can be applied to exploration of local transport and other functional phenomena in other spatially inhomogeneous systems.

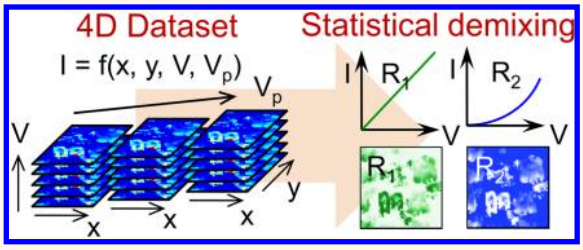

KEYWORDS: conduction hysteresis · oxide heterostructures · multivariate analysis · big data · scanning probe microscopy · FORC-IV

The complexity of the world around us stems primarily from the fact that materials, particles, and phenomena in it exist in a mixed, entwined form. Much of the technological progress from the Bronze Age metal smelting to modern crude oil refinement was focused on extraction of pure components from mixtures. Similarly, the power of science relies on the principle of explaining complex phenomena as originating from several simpler acts. One of the topical scientific challenges—data mining—is of the same nature. Whereas in the process of system characterization we can record voluminous multidimensional data sets, big data analysis becomes a serious problem. In this work we invoke the centuries-old paradigm of separation and address this issue by applying statistical methods to the task of demixing complex charge transport behavior in a two-component oxide nanocomposite.

Electronic transport in strongly correlated oxides has long been one of the key areas of condensed matter physics and is of interest to multiple technological applications.[1−5] It was long recognized that properties of these systems can be strongly position dependent and controlled by defects, interfaces, grain boundaries, and dislocations. The emergence of local scanning probe microscopy techniques[6−10] capable of addressing transport locally, on the level of individual interfaces, defects, or grain boundaries, has given a new impetus to the field and blossomed into a number of remarkable studies including 2D electron gas on oxide interfaces,[11,12] polarization-controlled tunneling in ferroelectric films,[13−16] conduction at grain boundaries, ferroelectric domain walls,[17−23] and 1D topological defects.[24] In all of these works, mechanisms associated with origins of disorder, local electronic transport, and bias-activated switching of different regimes were obtained from peculiarities in current−voltage (IV) curves.

Recently, it has been recognized that the electronic transport can be strongly affected by concurrent bias-induced electrochemical processes,[25−29] thermal or field

* Address correspondence to sergei2@ornl.gov, strelcove@ornl.gov.

Received for review April 11, 2014 and accepted May 28, 2014.

Published online May 28, 2014
10.1021/nn502029b

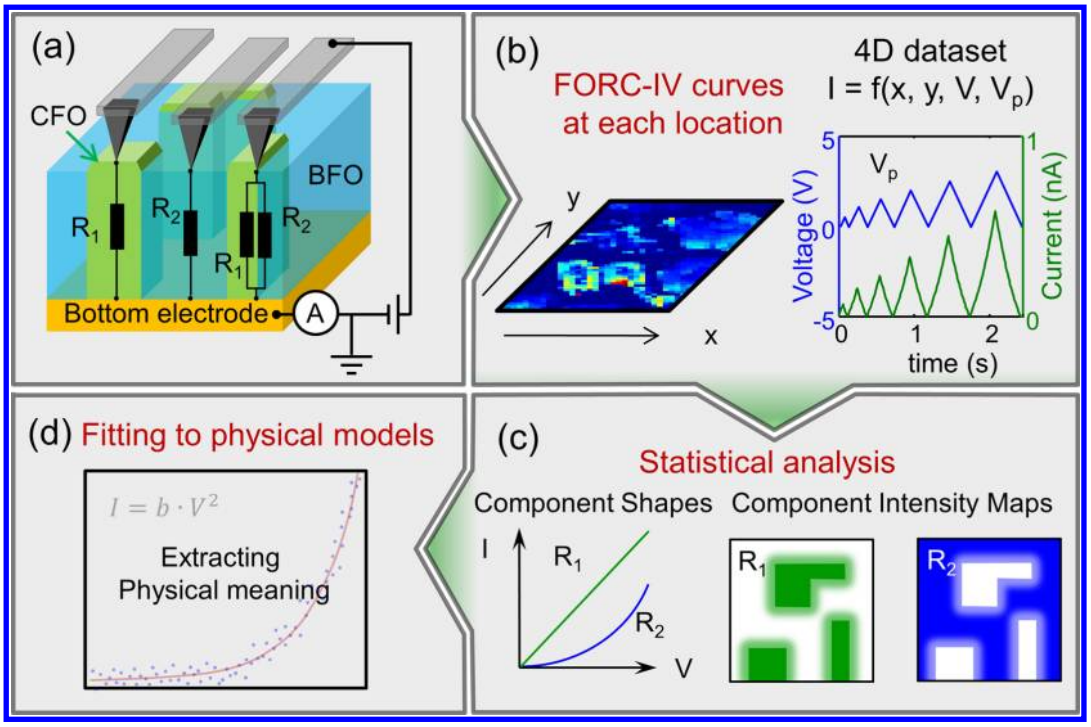

Figure 1. Experimental setup and data analysis flowchart. (a) Schematics of the CFO−BFO nanocomposite sample and FORC-IV experimental setup; IV curves measured over BFO and CFO regions can be modeled as different (non)linear resistors, whereas resistance on the CFO−BFO boundaries will be determined by both resistors connected in parallel. (b) A voltage waveform with several triangular pulses is applied at each spatial point of the sample, yielding a four-dimensional data set. (c) Information on the local behavior of IV curves becomes available via the statistical analysis of the FORC-IV data set. (d) The found components that represent typical material behavior can be fitted with specific physical models to yield quantitative information on its behavior.

metal−insulator transitions,[30−32] or ferroelectric polarization dynamics,[13,33,34] evoking complex time-dependent phenomena. A paradigmatic example is the interfacial or filament-controlled resistive switching in transition metal oxides, which is being actively explored in the context of neuromorphic and memristive electronics.[35−38] One characteristic facet of these systems is a complex field history dependence of conductance, controlled by bias-induced changes in chemical composition or polarization distribution. These convoluted processes, in turn, are controlled by surface structure with defects acting as nucleation and pinning centers.[39] Recently, we have introduced the first-order reversal curve current−voltage (FORC-IV) scanning probe microscopy (SPM) technique and demonstrated imaging on spatially uniform Ca-substituted $BiFeO_3$ and NiO systems[40,41] as well as interfacial electroresistance in the $BiFeO_3$−$CoFe_2O_4$ (BFO−CFO) nanocomposite.[42] Those studies show that the locally measured hysteresis in the FORC-IV curves corresponds to changes of electronic conduction sensed by the SPM in response to a bias-induced electrochemical process, with the area of the IV loop, or loop opening, acting as a measure of the local ionic activity.

One of the obstacles facing IV and FORC-IV spectroscopic imaging modes is data analysis and interpretation. Namely, only an insignificant fraction of the collected data is traditionally explored in the form of single local responses, or 2D cross sections, obviating the interpretation of physical behavior and extraction of information on local materials functionalities. For example, previously a spatially-resolved 4D FORC-IV data set, which consists of a measured current response for a bias waveform at a spatial pixel location, was analyzed to yield loop opening, threshold voltage, and minimal resistance at each peak bias,[40−42] leaving the bulk of the spatially and bias-dependent transport data unassessed. Similar hindrances plague other spectroscopic imaging modes, including 3D IV mapping in conductive atomic force microscopy (AFM) and continuous imaging tunneling spectroscopy in scanning tunneling microscopy. In this work, we combine FORC-IV measurements with multivariate statistical methods, to discriminate between different behaviors based on the *shapes* of the local IV curves in the full spectroscopic data set and use our data-driven interpretations to explore suitable physical models.

The essence of our approach is presented in Figure 1. FORC-IV data are acquired by recording current as a function of a positive bias voltage waveform (Figure 1b) applied to each pixel on a grid on the BFO−CFO sample surface (Figure 1a). The spectroscopic current data are then explored using multivariate statistics and clustering methods to determine the number of statistically significant dissimilar behaviors, yielding (a) the number of components

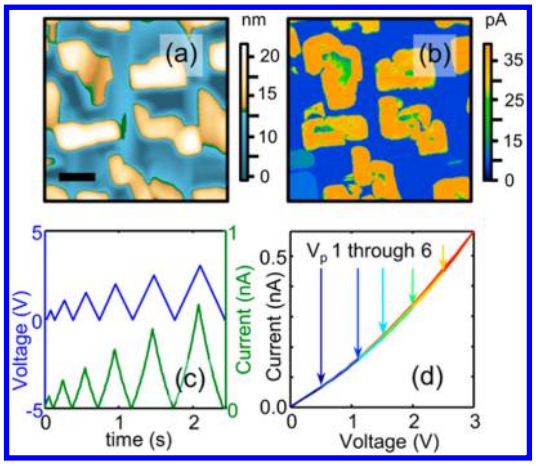

Figure 2. BFO–CFO nanocomposite. (a) Topographic image (scale bar is 100 nm). (b) CAFM image recorded at a tip bias of 0.1 V showing high interfacial conductance (in yellow). (c) FORC-IV voltage waveform and a typical current response. (d) Averaged set of FORC-IV curves recorded on region shown in (a) for a 50 × 50 spatial grid (2500 sets of IV curves in total); arrows show six peak bias values, the turning points of each of the six IV curves.

(behaviors), (b) components shapes (*e.g.*, representative IV curves in the case of FORC-IV data), and (c) intensity score maps of spatial distribution for each component. Figure 1c illustrates this for a simple case of a two-component system, with linear and nonlinear resistors. Here, local behavior can be modeled by sets of linear or nonlinear resistors connected in parallel; for example, interfacial resistance can be a combination of individual BFO and CFO resistors or conductivity channels corresponding to dissimilar carriers. In these cases, the component shape contains information on the physical mechanisms of local conduction and can be fitted to the appropriate physical model (Figure 1d). Overall, the multidimensional data set efficiently undergoes a lossless compression to several spatial maps of distinct statistically significant conductivity channels at a specific pixel location, thus visualizing local nanoscale properties of the sample. We will now proceed with the description of the CFO-BFO sample, FORC-IV measurements, statistical analysis, and physical parameters extraction in accordance with the scheme presented in Figure 1.

RESULTS AND DISCUSSION

Qualitative Analysis of Conductance in the BFO–CFO System. The CFO–BFO system is a self-assembled tubular heterostructure that forms spontaneously during pulsed laser deposition growth due to segregation of the perovskite BFO matrix and the CFO spinel inclusions.[43] The CFO nanopillars are approximately 100 nm across and show high interfacial conductivity at low tip biases (100 mV); however their cores, as well as the surrounding BFO matrix, are almost insulating (Figure 2a,b). Higher biases (7 to 8 V) lead to resistive switching in the interfaces; remarkably, the interfaces of a CFO island can be switched independently.[42] This behavior can be explained with a dynamic dopant model,[42,44,45] *i.e.*, coupling oxygen vacancies, concentrated at interfaces, and their motion in the external electric field with a related change of the doping level at a semiconducting interface and a subsequent formation of a p–n junction. The presence of interfacial ionic activity was also confirmed by FORC-IV.[42] However, due to very high variability in the type of transport between dissimilar locations, the mechanism of the electronic transport in this system remains ambiguous. In other words, spatial averages mix responses from different regions, whereas single pixel responses have low signal-to-noise ratios and their veracity is unclear. Here, we combine multivariate statistical analysis with physics-based fitting to analyze these behaviors systematically and reconstruct a comprehensive transport picture in these heterostructures.

FORC-IV data were collected on a 500 × 500 nm^2 region shown in Figure 2. A 50 × 50 grid was overlaid onto the area with each point probed by a bias waveform containing six triangular pulses going from 0 V to a peak bias value and back to 0 V. Peak bias (V_p) increased from 0.5 to 3 V in 0.5 V steps, forming six distinct triangular pulses (corresponding to six IV loops, Figure 2c). The spatially averaged IV curves show nonlinear behavior with diminutive hysteresis in the last two loops (Figure 2d). However, behavior at individual grid locations is drastically different: there are linear and nonlinear IV curves with different degrees of hysteresis starting at different threshold biases. Naturally questions arise, with regard to spatial variability and uniformity of these behaviors across material interfaces, whether these behaviors can be identified and if individual physical mechanisms can be determined.

The intrinsic four-dimensional nature of the FORC-IV data (current as a function of *x*, *y* position, voltage, and loop number) prevents the observer from immediately "seeing" spatial variation in behavior that is distributed over a 2D parameter space. One solution is to reduce the dimensionality to 3D, *e.g.*, extract area *vs* loop number, or average IV curve in the forward and reverse directions. These data sets can then be plotted as (*x*, *y*) cross sections (such as loop area maps) or spectra at individual points (see Figure S1 in the Supporting Information). We found that this simplification leads to partial losses of highly relevant information originally contained in the data. Indeed, the shapes of the local FORC-IV loops originate from the interplay of multiple physical mechanisms, such as local conduction and resistive switching. Additionally, besides the p–n junction mechanism mentioned above, these can include electrochemical processes of oxygen evolution and influence of surface states' population dynamics on the composite's conductivity (gas sensing effect[46]). Furthermore, local behavior can be strongly influenced by the degree of reversibility of the process responsible

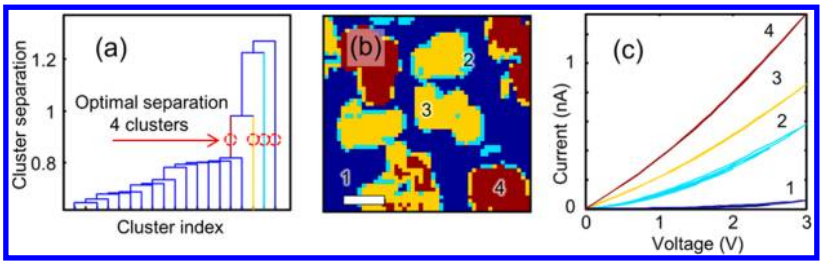

Figure 3. *k*-Means analysis of the FORC-IV data. (a) Dendrogram plot of hierarchial binary cluster tree showing that four is the optimal number of clusters (red circles). (b) *k*-Means cluster algorithm resultant map with four clusters specified (scale bar is 100 nm). (c) Mean FORC-IV curves for each of the four cluster types shown in map b.

for conduction and by stability of the tip−surface contact and instrument noise. Finally, whether these processes are controlled thermodynamically or kinetically is also irreducibly hidden in the full spectral data. Therefore, the need for a robust statistical approach capable of drawing conclusions from a complete data set free from compression loss becomes readily apparent.

Data Mining in FORC-IV. In order to decorrelate a high-dimensional FORC-IV data set in a way that allows physical interpretation, we need to know what is the smallest reasonable number of behaviors present in the system. The initial naïve hypothesis presented in Figure 1 was that the number of behaviors is equal to the number of materials in the nanocomposite. However, both the current map (Figure 2b) and FORC-IV loop area maps (Figure S1, Supporting Information) suggest a more complex scenario, with the interface manifesting a different kind of conductive behavior than the BFO and CFO regions. To help establish the relevant number of behaviors, we have employed a *k*-means clustering scheme on the full spectrographic data set.[47] The *k*-means algorithm separates *M* points that exist in *N* dimensions into a specified *k* number of clusters of curves that have similar behavior so that the sum of squares within a cluster is minimized.[48,49]

$$\arg\min \sum_{i=1}^{k} \sum_{x_j \in S_i} || x_j - \mu_i ||^2 \qquad (2)$$

Here μ_i is the mean of points in S_i. We have used a Matlab2012b version of the algorithm to minimize the sum over all clusters of the within-cluster sums of point-to-cluster-centroid distances. As a minimization parameter, we have used a square Euclidian distance with each centroid being the component-wise median of the points in a given cluster.

The *k*-means algorithm divides the data set in a specified number of optimally selected clusters. However, the number of clusters is *a priori* unknown. To get a measure of the quality of the separation as a function of the number of clusters, the data can be presented in the form of a dendrogram. The dendrogram plot in Figure 3a illustrates cluster arrangement in a top-down approach, where all observations are grouped into a single cluster initially and are recursively separated down the hierarchy. This is achieved by establishing a distance metric between observations and linkage criteria used to find the dissimilarity of clusters as a function of pairwise distances. As previously mentioned, we have used square Euclidian distance as our distance metric and centroid linkage, $||C_a - C_b||$, where C_a and C_b are the centroids of clusters *a* and *b*. That is to say, we look at how tight the information clusters in our data are as additional degrees of freedom are introduced. Therefore, a larger vertical drop in each of the binary branches, in Figure 3a, indicates a better cluster classification scheme in the data, where small changes offer only a marginally better reduction in the within-cluster sum. It then follows that minor vertical differences in the dendrogram plot can be dismissed, and the largest drops indicate major changes in data organization. Judging by the result shown in Figure 3a, we have concluded that separation of our data into *four* distinct types of behavior produces the most physically meaningful results. Therefore, we used four clusters as the inputs to our *k*-means clustering method.

k-Means clustering results are shown in Figure 3b, where each individual color represents a cluster. Figure 3c shows the mean IV for the entire data spectrogram, color coded with respect to the cluster it represents. The results show a trend in conduction behavior; the areas of highest conductivity with the least IV hysteresis are located within certain islands (red), with close second highest conductance being in other islands, shown in yellow. Closely following is the interface region shown in cyan. In this area we see some hysteresis and loop opening at higher peak biases. This trend continues with loops becoming continuously more hysteretic as we move to the BFO matrix (navy in Figure 3b).

As we augment our understanding of the internal structure in the data using *k*-means, the next natural step is to try to extract statistical behavior in a way that can be understood *physically*. That is to say, we want to separate our data into well-defined clusters with a clear spectroscopic behavior that has an intensity weight component providing insight into the spatial distribution of the behavior. Ideally, these components will also be physically viable, *i.e.*, well-behaved, positive, have additive weights, *etc.* This analysis can be achieved by Bayesian linear unmixing.[50] The Bayesian

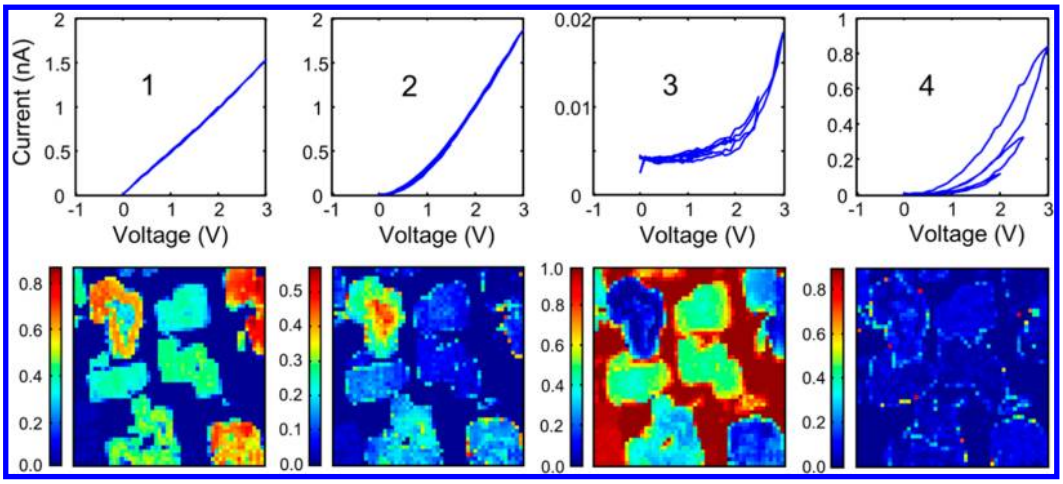

Figure 4. Bayesian analysis of the FORC-IV data. Top row: four Bayesian end-members; bottom row: corresponding Bayesian loading maps. Notice the rich internal structure of conductance within the grains as revealed in the Bayesian maps.

approach assumes data in a $Y = MA + N$ form, where the complete observations Y are a linear combination of position-independent endmembers, M, with respective relative abundances, A, corrupted by additive Gaussian noise N. Additional features and applicability of this method to extracting meaningful physical behavior out of end-members rely on non-negativity, full additivity, and sum-to-one constraints for both the end-members[51,52] and the abundance[53,54] coefficients.

The algorithm estimates the initial projection of end-members in a dimensionality-reduced subspace (PCA) *via* N-FINDR,[55] which finds a simplex of maximum volume that can be inscribed within the hyperspectral data set using a simple nonlinear inversion. The end-member abundance priors as well as noise variance priors are chosen by a multivariate Gaussian distribution, where the posterior distribution is calculated based on end-member independence using Markov chain Monte Carlo, which generates asymptotically distributed samples probed by Gibbs sampling strategy. The resulting end-members M are non-negative, and respective abundances add up to 1. Hence, the spectrum at each location is decomposed into a linear combination of spectra of individual components in corresponding proportions. Note that these particular constraints make transition from statistical analysis to physical behavior significantly more straightforward, as geometry of our sample implies a parallel combination of conduction channels (Figure 1), where currents are additive (more details in section III in the Supporting Information). By making the abundances additive and the end-members positive we can start assigning physical behavior to the shape and nature of the end-member curves. By extension, analysis of these curve's loading map adds the spatial component to the behavior that nonstatistical methods of analysis generally do not allow. An additional unique aspect of Bayesian analysis is that the end-member spectra and abundances are estimated jointly in a single step, unlike multiple least-squares regression methods, where initial spectra should be known.[50]

Bayesian deconvolution results are shown in Figure 4. They corroborate behavior shown by k-means, but also display a more detailed separation. Unlike the k-means map (Figure 3b), the image of the CFO island in the upper left corner of the Bayesian loading map strongly resembles the corresponding region in the CAFM map (Figure 2b), with the central part of the island and its interface having different conductivity. However, it is now evident that separation is not based purely on overall conductivity in the central and interfacial parts of this island, but rather on the shapes of the IV curves. The first Bayesian end-member, strongest on the island's interface (as well as two other islands), shows ohmic behavior, whereas the second Bayesian end-member is nonlinear and manifests mostly in the inner part of this island. The third end-member highlights the BFO matrix and has a very low current response, a current offset, and some loop opening. Finally, the last end-member is present only in a few of the interfacial points and can be described by a high conductivity and strongly hysteretic behavior. Thus, instead of separating conductivities of the BFO matrix and CFO islands (*i.e.*, trivial case, which even classical CAFM can resolve), Bayesian unmixing extracted four different types of behavior, ranging from ohmic to nonlinear to memristive. Simultaneously, by definition (positively defined and sum-to-one) Bayesian end-member spectra, on one hand, allow direct physical interpretation (*i.e.*, end-members are positive and scaled in nA) and, on the other hand, are different from the mean data found by k-means. Specifically, in cases when local transport can be represented as a superposition of parallel or series conductive channels, Bayesian components have direct meaning of individual components (see Supporting Information section III). The difference between the data averaged over some region and the strongest Bayesian end-member

TABLE 1. Possible Transport Mechanisms in BFO–CFO Nanocomposite[a]

Fowler–Nordheim tunneling	$I = S_{\text{eff}} \cdot \frac{q^3 m_{\text{Pt}}}{8\pi h m^* \varphi_B} E_{\max}{}^2 \, e^{-\sqrt{\frac{128\pi^2 m_s}{9h^2 q^2}} \varphi_B{}^3 E_{\max}}$
Schottky emission	$I = S_{\text{eff}} A^{**} T \, e^{-q\varphi_{B0}/kT} \, e^{-q/kT\left(\sqrt{\frac{qE_{\max}}{4\pi\varepsilon_s}}\right)}$
Poole–Frenkel conduction	$I = S_{\text{eff}} q\mu N_D E_{\text{bulk}} \, e^{\left[-\frac{q}{kT}\left(\varphi_B - \sqrt{\frac{qE_{\text{bulk}}}{\pi\varepsilon_s}}\right)\right]}$
Mott–Gurney law	$I = S_{\text{eff}} \frac{9\varepsilon\mu}{8d} E_{\text{bulk}}$
Child's law	$I = S_{\text{eff}} \frac{4\varepsilon}{9} \sqrt{\frac{2q}{m^* d}} E_{\text{bulk}}{}^3$

[a] S_{eff} is the effective tip–surface area; q is the elementary charge; m_{Pt} and m^* are effective electron masses in Pt and the semiconductor; h is the Planck's constant, ϕ_B is the barrier height; $E_{\max}$ is the maximal electric field in the metal–semiconductor interface; A^{**} is the effective Richardson constant; T is temperature; k is the Boltzmann constant; ε_s is the effective semiconductor permittivity; μ is the electron mobility in the semiconductor; N_D is the dopant concentration; E_{bulk} is the electric field in the semiconductor bulk; d is the sample thickness.

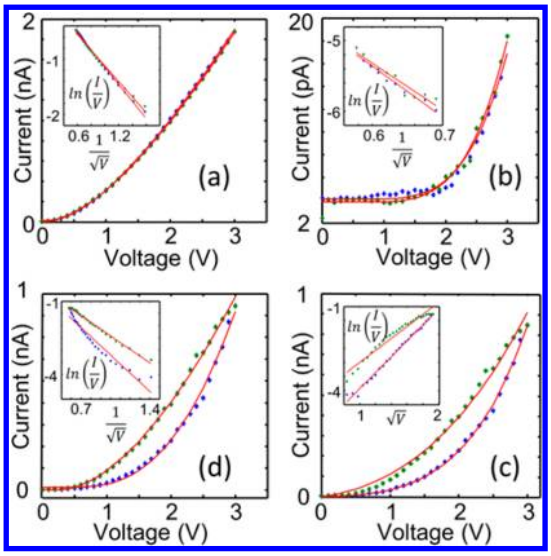

Figure 5. Fitting Bayesian end-members to different transport mechanisms. (a–c) Second, third, and fourth end-members fitted to the Fowler–Nordheim tunneling equation, correspondingly. d) Fourth end-member fitted to the Poole–Frenkel conduction model; blue and green crosses represent data for lower (forward) and upper (reverse) IV curves, correspondingly; best fits are shown in red lines. The insets show linearization of the curves in the corresponding normalized coordinates. Only the last loop at a peak bias of 3 V is shown for the sake of simplicity.

spectrum in this region can be understood intuitively as the difference between a mixture and one of its constituent components, as explained in Supporting Information (Figure S6). Here, we just point out that the Bayesian end-members highlight the most *representative component behavior*, rather than a simple average over the mix.

Physics behind Statistics. Having extracted the quintessential behaviors from the multidimensional data set, we now turn our attention to ascribing physical meaning to these behaviors. As suggested earlier (Figure 1), total local current through the BFO–CFO interface can be represented as a sum of currents through the constituent materials, which can be, therefore, associated with the Bayesian end-members that are also additive (see Supporting Information section III). Furthermore, the local electronic transport through the nanocomposite can be limited by either the electrode's surface junction, the conductance of the bulk, or a combination of the two. Table 1 summarizes the possible transport mechanisms, which we will compare to the Bayesian end-member spectra. The listed equations[16,56] were derived for a semiconductor in a uniform electric field, and therefore, in order to apply them to our tip–nanocomposite–bottom electrode system, we will employ the following assumptions: (1) for the cases of Fowler–Nordheim and Schottky emission mechanisms, we assume abrupt junction approximation,[56] with the maximal electric field in the tip–surface junction given by $E_{\max} = ((2q/\varepsilon_s)(V + V_{\text{bi}}))^{1/2}$, where V is the applied bias and V_{bi} is the built-in potential due to the difference between the metal and semiconductor work functions; (2) for the cases of Poole–Frenkel and space-charge-limited bulk conductance, we note that the local conductivity will strongly depend on the strength of the electric field, and therefore, current will be limited by the resistivity of the deep layers of the film, lying close to the bottom electrode, where electric field is the weakest and is proportional to the tip bias: $E_{\text{bulk}} = \alpha(V/d)$. COMSOL modeling shows that the field enhancement factor α is on the order of 10. It follows that none of the Bayesian end-members can be fitted well to the reverse-biased Schottky barrier emission equation (which could be the case for the positive tip bias; see bipolar IV curves in ref 42).

The second end-member can be equally well fitted to the space-charge-limited conductance and Fowler–Nordheim (FN) tunneling equations. Moreover, there is a transition in the voltage exponent from 1.6 to 2 as the peak bias increases (*i.e.*, from loop 1 to loop 6). However, the effective mass of the electron calculated from the Child's law fitting is too high to be physically meaningful. The electron mobility extracted from the Mott–Gurney law fit is *ca.* 6×10^{-4} cm^2/V·s, which is 9 orders of magnitude higher than the literature data for sintered powders[57,58] (3×10^{-13} cm^2/V·s at room temperature).

The FN fit of the second end-member is shown in Figure 5a. Data (except for the few low-bias points) are well linearized in the normalized logarithmic coordinates and yield a potential barrier of 0.3 meV. This value is reasonable, considering that the second end-member behavior is concentrated in the same CFO island as that of the first one, which is ohmic and lacks

any potential barrier at all. The third end-member can be satisfactorily fitted with the FN tunneling equation (Figure 5b), which, likewise, gives a low potential barrier of 0.5 meV.

The fourth end-member is set apart from the rest by the virtue of its hysteresis, with the forward and reverse IV curves having distinctively different shapes above a peak bias of *ca*. 2 V (*i.e*., last two loops). It is noteworthy that the upper IV branch of the fifth loop almost coincides with the lower branch of the next, sixth, loop, which is indicative of retention of higher conductivity after gradual switching. The natural question to ask is whether the conduction mechanism changes during this switching process. As Figure 5d and c show (see insets), the lower (forward) IV branch is best fitted by the Poole–Frenkel (PF) conductance, whereas the upper one (reverse) is consistent with the FN tunneling. We can speculate that the switching between the two mechanisms may be due to the oxygen vacancy redistribution activated at the interfacial regions and highlighted by this end-member. Initially, conductance is governed by the bulk PF transport, due to low bulk concentration of oxygen vacancies. Application of positive bias polarizes the BFO matrix and drives vacancies away from it, concentrating them on the outer part of the interface and decreasing local conductivity. Memristive switching occurs, and current henceforth is limited by the FN tunneling of the charge carriers from the metal-coated tip into the conduction band of the nanocomposite. Note, however, that the equations of Table 1 are derived under the immobile dopants assumption (bias-independent local dopant concentration), which is exactly the opposite of the mechanism underlying memristive behavior. The complexity of the nanoscale electrochemical processes makes it difficult to model it, and further studies are required to determine the exact mechanism behind the process manifested in the fourth Bayesian end-member. Finally, the first, ohmic, end-member can be used to estimate the conductivity of CFO, *ca*. 0.13 S/m, which is several orders of magnitude higher than reported before for pure CFO.[57] This is consistent with the hypothesis of oxygen vacancies being accumulated at the tubular BFO–CFO interface.[42] The interface becomes highly doped, almost metallic, which is detected experimentally and is reflected in the first Bayesian end-member (see Figure 4 left map).

Note that both the first and the fourth Bayesian end-members highlight the BFO–CFO interface, the inner and outer part thereof, respectively. In both instances oxygen vacancies presumably play the key role in the electronic transport behavior. However, the behaviors of the first and fourth end-members are strikingly different. An explanation for this can be found by recalling the dependence of semiconductor conductivity on dopant concentration. At low doping level, the semiconductor's electronic conductivity is low and very sensitive to small variations in doping level. A highly doped classical semiconductor, though, has a very high electronic conductivity, which does not change much in response to small variations in dopant concentration. Keeping in mind that oxygen vacancies act as a mobile dopant, whose concentration changes in response to the applied electric field, they will have a significant effect on the *local* electronic conductivity of CFO if their local concentration is medium-low. This is presumably the case of the outer CFO interface seen in the Bayesian loading map 4 (Figure 4). The inner part of the CFO islands, on the other hand, is highly doped, and its nearly metallic conductivity is insensitive to small changes in local oxygen dopant concentration. Therefore, the first end-member is nonhysteretic.

CONCLUSIONS AND OUTLOOK

In summary, we have studied a BFO–CFO nanocomposite by a combination of the FORC-IV technique and data mining analysis. It was established that in the explored experimental parameter space the conductive behavior of the composite is best described by four independent components: linear IV curves at the CFO–BFO interface, parabolic-exponential at the CFO island cores, exponential with low conductivity at the BFO matrix, and memristive at a few interfacial locations. These behaviors were explained in the framework of the model, where conductivity was controlled by the oxygen vacancies accumulated at the BFO–CFO interface, and the corresponding IV curves were fitted to different transport equations. It followed that the Fowler–Nordheim tunneling mechanism best describes conductivity of the BFO matrix, the core CFO island, and the upper part of the interfacial memristive curve, whereas Poole–Frenkel transport can explain the lower branch.

More generally, these studies establish the pathway for exploring complex position-dependent phenomena in inhomogeneous systems. While spectroscopic imaging techniques often allow spatially resolved responses to be measured, analysis and interpretation consistently remain a challenge. The combination of the statistical data mining approaches for identification of statistically significant behaviors and the physics-based fitting yields a powerful methodology for extracting physical meaning from a complex multidimensional data set.

METHODS

A BFO–CFO nanocomposite film of 100 nm was grown on 30 nm $SrRuO_3$ (SRO)-buffered $SrTiO_3$ (001) substrates by the pulsed lased deposition technique. Growth was monitored *in situ* using high-pressure reflective high-energy electron diffraction. Electrical measurements (CAFM and FORC-IV) were

performed on a Cypher AFM (Asylum Research) equipped with a National Instruments data acquisition card controlled by a computer through custom-written Matlab/LabView software. Bias was applied to a conductive Cr/Pt-coated (Budget Sensors) AFM tip, and current was detected off the bottom electrode (SRO) with a Femto amplifier (DLPCA-200). Matlab codes were used for data processing, statistical analysis, and fitting.

Conflict of Interest: The authors declare no competing financial interest.

Acknowledgment. This research was conducted at the Center for Nanophase Materials Sciences, which is sponsored at Oak Ridge National Laboratory by the Scientific User Facilities Division, Office of Basic Energy Sciences, U.S. Department of Energy. The work at National Chiao Tung University is supported by the National Science Council, R.O.C. (NSC-101-2119-M-009-003-MY2), Ministry of Education (MOE-ATU 101W961), and Center for Interdisciplinary Science of National Chiao Tung University.

Supporting Information Available: Figures S1−8 and descriptions thereof discuss loop area maps, principal component analysis of the FORC-IV data, applicability and limitations of Bayesian analysis, behavior of BFO−CFO interfaces, and contact area influence on the FORC-IV measurements. This material is available free of charge *via* the Internet at http://pubs.acs.org.

REFERENCES AND NOTES

1. Imada, M.; Fujimori, A.; Tokura, Y. Metal-Insulator Transitions. *Rev. Mod. Phys.* **1998**, *70*, 1039–1263.
2. Dagotto, E. Complexity in Strongly Correlated Electronic Systems. *Science* **2005**, *309*, 257–262.
3. Pentcheva, R.; Pickett, W. E. Electronic Phenomena at Complex Oxide Interfaces: Insights from First Principles. *J. Phys.: Condens. Matter* **2010**, *22*, 043001.
4. Jeong, D. S.; Thomas, R.; Katiyar, R. S.; Scott, J. F.; Kohlstedt, H.; Petraru, A.; Hwang, C. S. Emerging Memories: Resistive Switching Mechanisms and Current Status. *Rep. Prog. Phys.* **2012**, *75*, 076502.
5. Tsymbal, E. Y.; Kohlstedt, H. Tunneling across a Ferroelectric. *Science* **2006**, *313*, 181–183.
6. Kalinin, S. V.; Balke, N. Local Electrochemical Functionality in Energy Storage Materials and Devices by Scanning Probe Microscopies: Status and Perspectives. *Adv. Mater.* **2010**, *22*, E193–E209.
7. Kalinin, S.; Balke, N.; Jesse, S.; Tselev, A.; Kumar, A.; Arruda, T. M.; Guo, S. L.; Proksch, R. Li-Ion Dynamics and Reactivity on the Nanoscale. *Mater. Today* **2011**, *14*, 548–558.
8. Giridharagopal, R.; Shao, G. Z.; Groves, C.; Ginger, D. S. New SPM Techniques for Analyzing OPV Materials. *Mater. Today* **2010**, *13*, 50–56.
9. Gerber, C.; Lang, H. P. How the Doors to the Nanoworld Were Opened. *Nat. Nanotechnol.* **2006**, *1*, 3–5.
10. Bonnell, D. A.; Garra, J. Scanning Probe Microscopy of Oxide Surfaces: Atomic Structure and Properties. *Rep. Prog. Phys.* **2008**, *71*, 044501–1−4.
11. Ohtomo, A.; Hwang, H. Y. A High-Mobility Electron Gas at the $LaAlO_3/SrTiO_3$ Heterointerface. *Nature* **2004**, *427*, 423–426.
12. Herranz, G.; Basletić, M.; Bibes, M.; Carrétéro, C.; Tafra, E.; Jacquet, E.; Bouzehouane, K.; Deranlot, C.; Hamzić, A.; Broto, J. M.; *et al.* High Mobility in $LaAlO_3/SrTiO_3$ Heterostructures: Origin, Dimensionality, and Perspectives. *Phys. Rev. Lett.* **2007**, *98*, 216803–216807.
13. Maksymovych, P.; Jesse, S.; Yu, P.; Ramesh, R.; Baddorf, A. P.; Kalinin, S. V. Polarization Control of Electron Tunneling into Ferroelectric Surfaces. *Science* **2009**, *324*, 1421–1425.
14. Garcia, V.; Fusil, S.; Bouzehouane, K.; Enouz-Vedrenne, S.; Mathur, N. D.; Barthelemy, A.; Bibes, M. Giant Tunnel Electroresistance for Non-Destructive Readout of Ferroelectric States. *Nature* **2009**, *460*, 81–84.
15. Gruverman, A.; Wu, D.; Lu, H.; Wang, Y.; Jang, H. W.; Folkman, C. M.; Zhuravlev, M. Y.; Felker, D.; Rzchowski, M.; Eom, C. B.; *et al.* Tunneling Electroresistance Effect in Ferroelectric Tunnel Junctions at the Nanoscale. *Nano Lett.* **2009**, *9*, 3539–3543.
16. Maksymovych, P.; Pan, M. H.; Yu, P.; Ramesh, R.; Baddorf, A. P.; Kalinin, S. V. Scaling and Disorder Analysis of Local I-V Curves from Ferroelectric Thin Films of Lead Zirconate Titanate. *Nanotechnology* **2011**, *22*.
17. Seidel, J.; Martin, L. W.; He, Q.; Zhan, Q.; Chu, Y. H.; Rother, A.; Hawkridge, M. E.; Maksymovych, P.; Yu, P.; *et al.* Conduction at Domain Walls in Oxide Multiferroics. *Nat. Mater.* **2009**, *8*, 229–234.
18. Maksymovych, P.; Seidel, J.; Chu, Y. H.; Wu, P. P.; Baddorf, A. P.; Chen, L. Q.; Kalinin, S. V.; Ramesh, R. Dynamic Conductivity of Ferroelectric Domain Walls in $BiFeO_3$. *Nano Lett.* **2011**, *11*, 1906–1912.
19. Maksymovych, P.; Morozovska, A. N.; Yu, P.; Eliseev, E. A.; Chu, Y. H.; Ramesh, R.; Baddorf, A. P.; Kalinin, S. V. Tunable Metallic Conductance in Ferroelectric Nanodomains. *Nano Lett.* **2012**, *12*, 209–213.
20. Farokhipoor, S.; Noheda, B. Conduction through 71 Degrees Domain Walls in $BiFeO_3$ Thin Films. *Phys. Rev. Lett.* **2011**, *107*, 126701–1−4.
21. Guyonnet, J.; Gaponenko, I.; Gariglio, S.; Paruch, P. Conduction at Domain Walls in Insulating $Pb(Zr_{0.2}Ti_{0.8})O_3$ Thin Films. *Adv. Mater.* **2011**, *23*, 5377–5381.
22. Wu, W. D.; Horibe, Y.; Lee, N.; Cheong, S. W.; Guest, J. R. Conduction of Topologically Protected Charged Ferroelectric Domain Walls. *Phys. Rev. Lett.* **2012**, *108*, 077203–1−3.
23. Wu, W. D.; Guest, J. R.; Horibe, Y.; Park, S.; Choi, T.; Cheong, S. W.; Bode, M. Polarization-Modulated Rectification at Ferroelectric Surfaces. *Phys. Rev. Lett.* **2010**, *104*, 217601–1−5.
24. Balke, N.; Winchester, B.; Ren, W.; Chu, Y. H.; Morozovska, A. N.; Eliseev, E. A.; Huijben, M.; Vasudevan, R. K.; Maksymovych, P.; Britson; *et al.* Enhanced Electric Conductivity at Ferroelectric Vortex Cores in $BiFeO_3$. *Nat. Phys.* **2012**, *8*, 81–88.
25. Mannhart, J.; Schlom, D. G. Oxide Interfaces-An Opportunity for Electronics. *Science* **2010**, *327*, 1607–1611.
26. Sawa, A. Resistive Switching in Transition Metal Oxides. *Mater. Today* **2008**, *11*, 28–36.
27. Szot, K.; Rogala, M.; Speier, W.; Klusek, Z.; Besmehn, A.; Waser, R. TiO_2 - a Prototypical Memristive Material. *Nanotechnology* **2011**, *22*, 254001–254022.
28. Waser, R.; Dittmann, R.; Staikov, G.; Szot, K. Redox-Based Resistive Switching Memories - Nanoionic Mechanisms, Prospects, and Challenges. *Adv. Mater.* **2009**, *21*, 2632–2645.
29. Strukov, D. B.; Snider, G. S.; Stewart, D. R.; Williams, R. S. The Missing Memristor Found. *Nature* **2008**, *453*, 80–83.
30. Strelcov, E.; Lilach, Y.; Kolmakov, A. Gas Sensor Based on Metal−Insulator Transition in VO_2 Nanowire Thermistor. *Nano Lett.* **2009**, *9*, 2322–2326.
31. Nakano, M.; Shibuya, K.; Okuyama, D.; Hatano, T.; Ono, S.; Kawasaki, M.; Iwasa, Y.; Tokura, Y. Collective Bulk Carrier Delocalization Driven by Electrostatic Surface Charge Accumulation. *Nature* **2012**, *487*, 459–462.
32. Hormoz, S.; Ramanathan, S. Limits on Vanadium Oxide Mott Metal−Insulator Transition Field-Effect Transistors. *Solid-State Electron.* **2010**, *54*, 654–659.
33. Gruverman, A. Nanoscale Insight into the Statics and Dynamics of Polarization Behavior in Thin Film Ferroelectric Capacitors. *J. Mater. Sci.* **2009**, *44*, 5182–5188.
34. Crassous, A.; Bernard, R.; Fusil, S.; Bouzehouane, K.; Briatico, J.; Bibes, M.; Barthélémy, A.; Villegas, J. E. $BiFeO_3/YBa_2Cu_3O_{7-\delta}$ Heterostructures for Strong Ferroelectric Modulation of Superconductivity. *J. Appl. Phys.* **2013**, *113*, 024910−1−3.
35. Ha, S. D.; Ramanathan, S. Adaptive Oxide Electronics: A Review. *J. Appl. Phys.* **2011**, *110*, 071101.
36. Jo, S. H.; Chang, T.; Ebong, I.; Bhadviya, B. B.; Mazumder, P.; Lu, W. Nanoscale Memristor Device as Synapse in Neuromorphic Systems. *Nano Lett.* **2010**, *10*, 1297–1301.
37. Likharev, K. K. Hybrid CMOS/Nanoelectronic Circuits: Opportunities and Challenges. *J. Nanoelectron. Optoelectron.* **2008**, *3*, 203–230.

38. Waser, R. *Nanoelectronics and Information Technology*; Wiley-VCH, 2012.
39. Kwon, D. H.; Kim, K. M.; Jang, J. H.; Jeon, J. M.; Lee, M. H.; Kim, G. H.; Li, X. S.; Park, G. S.; Lee, B.; *et al*. Atomic Structure of Conducting Nanofilaments in TiO_2 Resistive Switching Memory. *Nat. Nanotechnol.* **2010**, *5*, 148–153.
40. Strelcov, E.; Kim, Y.; Jesse, S.; Cao, Y.; Ivanov, I. N.; Kravchenko, I. I.; Wang, C. H.; Teng, Y. C.; Chen, L. Q.; Chu, Y. H.; Kalinin, S. V. Probing Local Ionic Dynamics in Functional Oxides at the Nanoscale. *Nano Lett.* **2013**, *13*, 3455–3462.
41. Kim, Y.; Strelcov, E.; Hwang, I. R.; Choi, T.; Park, B. H.; Jesse, S.; Kalinin, S. V. Correlative Multimodal Probing of Ionically-Mediated Electromechanical Phenomena in Simple Oxides. *Sci. Rep.* **2013**, *3*, 2924−1–7.
42. Hsieh, Y.-H.; Strelcov, E.; Liou, J.-M.; Shen, C.-Y.; Chen, Y.-C.; Kalinin, S. V.; Chu, Y.-H. Electrical Modulation of the Local Conduction at Oxide Tubular Interfaces. *ACS Nano* **2013**, *7*, 8627–8633.
43. Hsieh, Y. H.; Liou, J. M.; Huang, B. C.; Liang, C. W.; He, Q.; Zhan, Q.; Chiu, Y. P.; Chen, Y. C.; Chu, Y. H. Local Conduction at the $BiFeO_3$-$CoFe_2O_4$ Tubular Oxide Interface. *Adv. Mater.* **2012**, *24*, 4564–4568.
44. Cahen, D.; Chernyak, L.; Dagan, G.; Jakubowicz, A. Ion Mobility in Chalcogenide Semiconductors - Room Temperature Creation of Bipolar Junction Transistor. *Fast Ion Transport in Solids*; Scrosati, B.; Magistris, A.; Mari, C. M.; Mariotto, G., Eds.; Kluwer Academic Publ: Dordrecht, 1993; Vol. 250, pp 121−141.
45. Cahen, D.; Chernyak, L. Dopant Electromigration in Semiconductors. *Adv. Mater.* **1997**, *9*, 861–867.
46. Comini, E.; Faglia, G.; Sberveglieri, G. *Solid State Gas Sensing*; Springer Science & Business Media: New York, 2008.
47. Haykin, S. S. *Neural Networks: A Comprehensive Foundation*; Prentice Hall, 1999.
48. Hartigan, J. A.; Wong, M. A. Algorithm AS 136: A K-Means Clustering Algorithm. *J. R. Stat. Soc. C (Appl. Stat.)* **1979**, *28*, 100–108.
49. MacQueen, J. B. Some Methods for Classification and Analysis of MultiVariate Observations. *Proceedings of the Fifth Berkeley Symposium on Mathematical Statistics and Probability*; Cam, L. M. L.; Neyman, J., Eds.; University of California Press, 1967; Vol. 1, pp 281−297.
50. Dobigeon, N.; Moussaoui, S.; Coulon, M.; Tourneret, J. Y.; Hero, A. O. Joint Bayesian Endmember Extraction and Linear Unmixing for Hyperspectral Imagery. *Signal Processing, IEEE Trans. on* **2009**, *57*, 4355–4368.
51. Moussaoui, S.; Brie, D.; Mohammad-Djafari, A.; Carteret, C. Separation of Non-Negative Mixture of Non-Negative Sources Using a Bayesian Approach and MCMC Sampling. *IEEE Trans. Signal Process.* **2006**, *54*, 4133–4145.
52. Dobigeon, N.; Moussaoui, S.; Tourneret, J. Y. Blind Unmixing of Linear Mixtures Using a Hierarchical Bayesian Model. Application to Spectroscopic Signal Analysis. *Proceeding of the IEEE-SP Workshop Statistics and Signal Processing*; Madison, WI, **2007**; pp 79−83.
53. Parra, L.; Mueller, K.-R.; Spence, C.; Ziehe, A.; Sajda, P. Unmixing Hyperspectral Data. *Adv. Neural Inf. Proc. Syst. (NIPS)* **2000**, *12*, 942–948.
54. Dobigeon, N.; Tourneret, J. Y.; Chein, I. C. Semi-Supervised Linear Spectral Unmixing Using a Hierarchical Bayesian Model for Hyperspectral Imagery. *IEEE Trans. Signal Process.* **2008**, *56*, 2684–2695.
55. Winter, M. E. N-FINDR: an Algorithm for Fast Autonomous Spectral Endmember Determination in Hyperspectral Data. *Proc. SPIE* **1999**, 266−275.
56. Sze, S. M. *Physics of Semiconductor Devices*, 2nd ed.; John Wiley & Sons: New York, NY, 1981; p 868.
57. Selim, M. S.; Turky, G.; Shouman, M. A.; El-Shobaky, G. A. Effect of Li_2O Doping on Electrical Properties of $CoFe_2O_4$. *Solid State Ionics* **1999**, *120*, 173–181.
58. Ishtiaq, A.; Muhammad, T. F. Characterization of Cobalt Based Spinel Ferrites with Small Substitution of Gadolinium. *World Appl. Sci. J.* **2012**, *19*, 464–469.